Prediction of Broadband Blade-Wake Back-Scatter Noise from a Hovering Ideally Twisted Rotor using OVERFLOW2-ANOPP2

Christopher S. Thurman*, D. Douglas Boyd Jr.†, Leonard V. Lopes‡
NASA Langley Research Center, Hampton, VA, 23681

This work illustrates the use of a hybrid RANS/LES framework for the prediction of broadband noise via integral formulations from an ideally twisted hovering rotor. Four simulations were conducted, which investigated the effect of different turbulence modeling and spatiotemporal resolutions. The aerodynamic performance and aeroacoustics predicted by these four computational cases were compared against data acquired in the Small Hover Anechoic Chamber at the NASA Langley Research Center and against previous simulations conducted using the lattice-Boltzmann solver, PowerFLOW. The simulation case with the finest spatial resolution had the most favorable aerodynamic performance and broadband noise comparison with measured data; however, the simulation case utilizing the SST-DDES turbulence model predicted the most accurate tonal noise signature. Aerodynamic flowfield visualizations identified near-wake trailing edge vortex shedding, perpendicular blade-vortex interactions, and tip vortex formation, which are known to cause broadband noise. The fluid dynamics associated with a new broadband noise source, blade-wake back-scatter, were also identified. Lastly, a broadband noise source visualization technique was utilized to confirm the presence of blade-wake back-scatter as a dominant broadband noise source.

Nomenclature

c	=	rotor blade chord length, m
c_∞	=	freestream speed of sound, m/s
G_{xx}	=	power spectral density, Pa^2/Hz
M	=	local Mach number
M_r	=	local Mach number in the direction of acoustic observer
M_{tip}	=	Mach number at the rotor blade tip
N_b	=	number of rotor blades
$\hat{\mathbf{n}}$	=	surface normal vector
PSD	=	power spectral density, dB/Hz
$\dot{p}$	=	source time derivative of surface pressure, Pa/s
p_{ref}	=	reference pressure, 20 μPa
p'_{UL}	=	unsteady loading acoustic pressure, Pa
R	=	rotor radius, m
Re_{tip}	=	Reynolds number at the rotor blade tip
r	=	rotor blade span location normalized by rotor radius
r_d	=	distance between emission location and observer at reception time, m
SPL	=	sound pressure level, dB
$\text{SPL}_{1/3}$	=	one-third octave sound pressure level, dB
t_{obs}	=	observer time, s
$\mathbf{x}_{obs}$	=	observer location, m
y	=	radial observer location relative to the center of rotor rotation normalized by R
$\mathbf{y}_{src}$	=	source location, m
y^+	=	normalized wall distance

*Research Aerospace Engineer, Aeroacoustics Branch, MS 461, AIAA Member; christopher.thurman@nasa.gov
†Senior Research Aerospace Engineer, Aeroacoustics Branch, MS 461, AIAA Associate Fellow; d.d.boyd@nasa.gov
‡Senior Research Aerospace Engineer, Aeroacoustics Branch, MS 461, AIAA Senior Member; leonard.v.lopes@nasa.gov

Δf = narrowband spectra frequency resolution, Hz
Δs_1 = isotropic grid spacing in first off-body grid and adaptive mesh refinement region, m
Δt = flow solver time step, deg
Δt_s = time step for flow solver data sampling, deg
Δx = grid spacing in the chordwise direction, m
Δy = grid spacing in the wall-normal direction, m
Δz = grid spacing in the spanwise direction, m
Θ_{obs} = observer angle relative to rotor plane, deg
θ = local angle between surface normal and radiation direction, deg
τ = emission time, s
Ω = rotor speed, RPM
ω = vorticity, 1/s

I. Introduction

The past decade has seen considerable interest in advanced air mobility (AAM) vehicles, capable of transporting personnel and packages across various environments in a safe and sustainable way. These vehicles are typically comprised of multirotor systems and generally range in size from small unmanned aerial systems (sUAS) to single- or multipassenger vehicles designed for operation in urban environments. Though the AAM industry is growing at a rapid pace, noise is still a concern for the development and real-world application of these AAM vehicles. Designing AAM vehicles for public acceptance has motivated research in identifying and characterizing noise sources produced by sUAS vehicles, such as quadcopters. The study of these smaller sUAS vehicles, or isolated sUAS vehicle components such as rotors, can not only aid in the design of low-noise AAM vehicles, but also in mission planning and trajectory optimization.

The difference in size of these sUAS vehicles, when compared to traditional helicopters, has shown a paradigm shift in the relative importance of different noise-generating mechanisms. For example, it has been shown that the stochastic, or broadband, portion of the noise emanating from sUAS vehicles lies in the most perceptible range of human audibility and is a dominant noise source when compared to the deterministic, or tonal, noise [1, 2]. This is in contrast to traditional helicopters, where tonal noise dominates over broadband, and, for this reason, limited work has been done in the prediction and analysis of broadband noise until recently.

There are three types of rotor broadband noise: blade self-noise, turbulence ingestion noise (TIN), and blade-wake interaction (BWI) noise. Blade self-noise, typically produced by near-wake turbulence scattering over a rotor blade trailing edge (i.e., boundary layer dependent), has been studied and modeled extensively [1, 3–10]. TIN, caused by the ingestion of atmospheric turbulence into the rotor system, is typically seen in outdoor testing environments [11] and is thought to be prevalent in real-world operation. BWI noise can be loosely defined as noise caused by blade interactions with blade-wake turbulence. The blade-wake turbulence associated with BWI noise is entrained in blade-tip vortices and interacts with subsequent blades in a perpendicular fashion, elucidating the frequently used synonymous term, perpendicular blade-vortex interaction (BVI) noise, in lieu of BWI noise.

Many tools exist for predicting both tonal and broadband noise [1, 2, 5, 8]. Modeling tonal noise typically entails an aerodynamic calculation to compute blade aerodynamic forces and kinematics and an acoustic propagation code to predict the noise at an observer location. For the aerodynamic calculation, a wide range of tools with varying fidelity exist: panel methods, blade element momentum theory (BEMT), comprehensive analysis codes (e.g., CAMRAD II, CHARM, and RCAS), traditional Navier-Stokes solvers (e.g., OVERFLOW2 and FUN3D), and scale-resolving flow simulations (e.g., direct numerical simulation and large eddy simulation). Each of these tools is used to predict unsteady aerodynamic forces, which are in turn used to predict acoustic pressure at an observer location using an implementation of the Ffowcs Williams and Hawkings (FW-H) [12] equation. Similar approaches have been used to predict broadband noise directly from unsteady aerodynamic forces using the scale-resolving lattice-Boltzmann method, though at great computational cost [2, 8, 13, 14].

To date, there is much ambiguity surrounding the prediction of rotor broadband noise using finite-volume Navier-Stokes solvers. Hybrid Reynolds-averaged Navier-Stokes (RANS)/large eddy simulation (LES) paradigms are the workhorse finite-volume methods implemented for practical engineering problems; however, the boundary layer is often assumed to be fully turbulent and is modeled using RANS-based turbulence models. This assumption is counterintuitive to the prediction of broadband self-noise sources such as turbulent boundary layer trailing edge (TBLTE) noise, since the noise-producing energetic turbulence in the outer region of the boundary layer is being modeled and not resolved.

This limitation is not unique to hybrid RANS/LES paradigms and was shown to also be problematic when using wall-functions unless some triggering mechanism (e.g., boundary layer trip) was used to activate the scale-resolving modality in the boundary layer [13–15]. However, it may be argued that when external turbulence is present, such as blade wake entrained by tip vortices (i.e., BWI noise), accurate broadband noise predictions can be attained. This was shown in Ref. [8] using a lattice-Boltzmann solver for a hovering ideally twisted rotor (ITR) geometry with broadband BWI noise caused by perpendicular BVIs.

The purpose of the current work is to predict broadband noise using OVERFLOW2, a structured Navier-Stokes solver, as the aerodynamic solver for the hovering ITR of Refs. [8] and [9]. A hybrid RANS/LES approach will be utilized and the effects of using different RANS-based turbulence models and different spatiotemporal resolutions will be investigated. Aerodynamic and acoustic results will be compared to measured results from the Small Hover Anechoic Chamber (SHAC) facility at the NASA Langley Research Center as well as to the predictions performed in Ref. [8] using the lattice-Boltzmann solver, PowerFLOW. Lastly, broadband noise source localization and visualization techniques will be used and a new broadband noise source, blade-wake back-scatter, will be identified for the first time.

II. Technical Approach

This work investigated four computational cases to study the effect of different numerical parameters on broadband noise prediction. Section II.A will discuss the rotor geometry and only the baseline case will be discussed in Sections II.B and II.C unless otherwise specified. Section II.D will then detail the numerical parameters associated with the other three cases.

A. Rotor Design

The rotor utilized in this work was the four-bladed ($N_b = 4$) ITR documented in Refs. [8] and [9], which is shown in Fig. 1. The ITR has a radius of $R = 0.15875$ m, uses an NACA 0012 airfoil profile along the blade span, and has a constant chord length of $c = 0.0254$ m with a blunt trailing edge measuring $0.0157c$. It was designed using BEMT to produce 11.12 N of thrust at a rotor speed of $\Omega = 5500$ RPM. Further details of the ITR design can be found in Ref. [9].

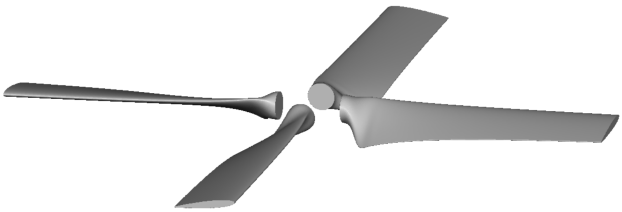

Fig. 1 Ideally twisted rotor geometry.

B. Geometry Discretization

OVERFLOW2 uses an overlapping grid framework, so each ITR blade consisted of three surface grids: one encompassing the main portion of the blade and two on the tip and root end caps, which overlap the main blade grid. Figure 2 shows the three overlapping surface grids, where the grid lines of the two overlapping grids are shown in red and the grid lines for the main blade are shown in black. All surface and near-body grids were generated using Chimera Grid Tools [16]. There were 271 grid points in the spanwise direction, with a mean cell length of $\Delta z = 5.59 \times 10^{-4}$ m and root and tip spacings of $\Delta z = 1.00 \times 10^{-4}$ m. The chordwise direction had 221 grid points around the airfoil, with leading and trailing edge spacings of $\Delta x = 3.99 \times 10^{-5}$ m, an average grid spacing of $\Delta x = 3.00 \times 10^{-4}$ m, and 25 points around the blunt trailing edge.

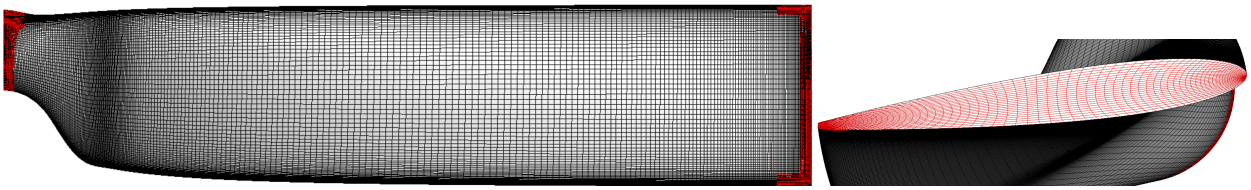

(a) Top view. **(b) Side view.**

Fig. 2 Ideally twisted rotor surface grids.

A volumetric near-body O-grid was extruded from each of the overlapping surface grids with an initial wall-normal

spacing of $\Delta y = 1.00 \times 10^{-6}$ m, which corresponds to a y^+ spacing of 0.3 at the blade tip. The O-grids were hyperbolically marched approximately $1.25c$ away from the blade in the wall-normal direction and consisted of 91 grid points, with an end spacing of $\Delta y = 0.00150$ m, or roughly $0.05c$. The Domain Connectivity Function (DCF) process was used to generate all off-body volumetric grids. The first off-body grid, in which the blades and near-body grids were located, extended approximately $1.2R$ away from the axis of rotation in the spanwise directions and extended $0.3R$ in the positive and negative vertical directions from the center of the rotor. This first off-body grid had a grid spacing of $\Delta s_1 = 0.05c$. After the coarse time-step startup, which will be discussed in the next section, off-body adaptive mesh refinement (AMR) [17] was used every two time steps to adapt the grid spacing to $\Delta s_1 = 0.05c$ in a region extending $3R$ in the negative vertical direction using the undivided second squared difference of the conserved Navier-Stokes flow variables (i.e., density, momentum, and energy). The near-body and off-body grids are shown in Fig. 3, where Fig. 3b shows the first off-body grid and AMR region.

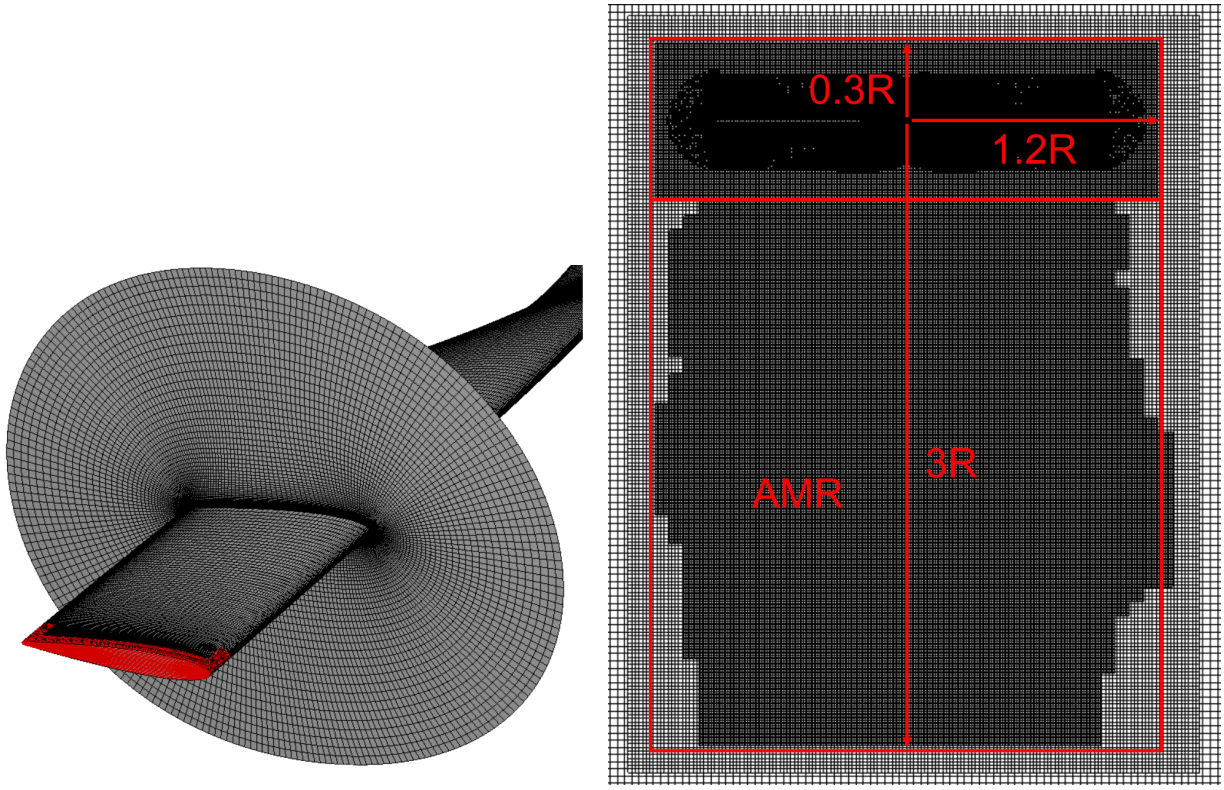

(a) O-grid. **(b) Off-body grids.**

Fig. 3 Volumetric grid illustrations.

C. Numerical Methods

OVERFLOW2 is a structured grid Navier-Stokes solver, which employs an overlapping grid methodology [18]. Full OVERFLOW2 details can be found in Ref. [19] and will be excluded herein for brevity. The discretization discussed in the previous section and the numerical methods discussed subsequently follow best practices determined by Chaderjian [20] for isolated hovering rotor simulations using OVERFLOW2.

The operating condition investigated in this work was the ITR design hover condition of $\Omega = 5500$ RPM, which corresponds to a blade tip Mach number and Reynolds number of $M_{\text{tip}} = 0.269$ and $Re_{\text{tip}} = 1.98 \times 10^5$, respectively. To solve the unsteady Navier-Stokes equations, a dual-time approach was utilized, where the improved Einfeldt's version of the Harten, Lax, and van Leer (HLLE++) upwind algorithm [21] and fifth-order spatial differencing was used with an improved implicit symmetric successive over relaxation (SSOR) solver [22] to sufficiently reduce the pseudo time integration error at each time step. An optimized second-order backward differencing scheme (BDF2OPT) was used for the temporal integration with a physical time step correspondent to $\Delta t = 0.25°$, or 1440 steps per rotor revolution.

A hybrid RANS/LES framework was used in this work for all simulation cases where the Boussinesq assumption relates the Reynolds stress in the governing RANS equations to a mean strain-rate tensor and turbulent eddy viscosity calculated using turbulence model-based closures. Delayed detached eddy simulations (DDES) were used, which effectively switch between a RANS-based turbulence model in the boundary layer and a Smagorinsky-type LES elsewhere in the computational domain. Two DDES formulations were investigated in this work. The first was the standard DDES [23] using the negative variant of the one-equation Spalart-Allmaras turbulence model with a rotation/curvature correction (SA-neg-noft2-RC), which will hereby be denoted as SA-DDES. The second DDES formulation was that of Gritskevich et al. [24] which used the two-equation $k-\omega$ shear stress transport (SST) turbulence model, also with a rotation/curvature correction (SST-RC), denoted as SST-DDES.

AMR was used every two time steps (i.e., $\Delta t = 0.50°$) in the region shown in Fig. 3b. Approximately 20 subiterations were solved at each time step to reduce the subiteration residual by 2.5 orders of magnitude. A quick-start procedure was employed without AMR where a coarse time step of $\Delta t = 2.5°$ was used to simulate ten rotor revolutions for the stabilization of start-up transients. After these first ten rotor revolutions in the quick-start procedure, five additional revolutions were simulated at $\Delta t = 0.25°$ before outputting unsteady surface pressure data every two time steps (i.e., $\Delta t_s = 0.50°$) for acoustic calculations. Thrust and torque convergence trends for the first 15 rotor revolutions are shown in Fig. 4.

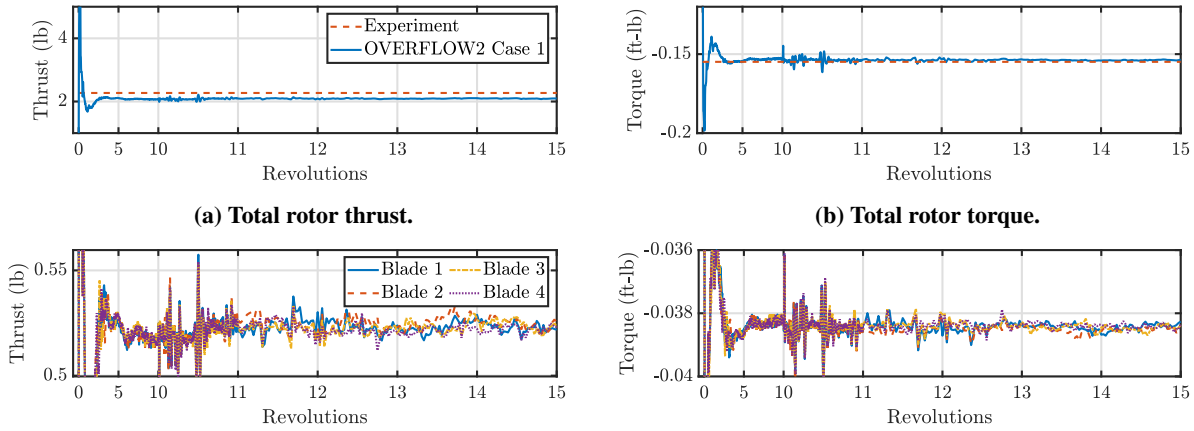

(a) Total rotor thrust.

(b) Total rotor torque.

(c) Thrust component contribution.

(d) Torque component contribution.

Fig. 4 Convergence trends over the first 15 rotor revolutions.

Each rotor revolution simulated at a time step of $\Delta t = 0.25°$ took approximately 700 CPU hours. It should be noted that when using AMR, the frequency for outputting unsteady surface pressures should be identical to the AMR frequency, otherwise the adapted off-body grids will be frozen at a time step which is inconsistent with the flow solution at the instance of data extraction.

D. Simulation Cases

The key parameters associated with each case are shown in Table 1. Case 1 is the baseline simulation case that has been detailed previously. Case 2 utilized the SST-DDES turbulence model in lieu of the SA-DDES used by the baseline simulation. Case 3 investigated the effect of increasing the temporal resolution from the baseline case. For Case 3, the simulation time step remained consistent with the baseline case at $\Delta t = 0.25°$, however, the unsteady surface pressures were output every time step (i.e., $\Delta t_s = 0.25°$), rather than every two time steps like with the baseline case. To accommodate this increased sampling frequency, AMR was also performed every time step for Case 3. Case 4 investigated the effect of increasing the spatial resolution. The near-body grids for Case 4 remained consistent with the baseline simulation, however, the first off-body grid and AMR region shown in Fig. 3b had an increased spatial resolution of $\Delta s_1 = 0.025c$.

Table 1 Simulation parameters.

Case	Δt_s	Δs_1	Turbulence Model
1 (baseline)	0.50°	$0.050c$	SA-DDES
2	0.50°	$0.050c$	SST-DDES
3	0.25°	$0.050c$	SA-DDES
4	0.50°	$0.025c$	SA-DDES

E. Acoustic Post-Processing

Unsteady blade loading was sampled over ten revolutions at a rate of 132 kHz (i.e., $\Delta t_s = 0.25°$) for Case 3 and 66 kHz (i.e., $\Delta t_s = 0.50°$) for all other simulation cases. These sampled data were then provided to the ANOPP2 [25] Computational Fluid Dynamics (CFD) Acoustic Propagation Tool (ACAPT) for the computation of propagated acoustic pressure time history (APTH) at a defined observer location using the impermeable Farassat's Formulation 1A (F1A) [26–28]. ACAPT was used to propagate the APTH from the impermeable rotor blade surfaces to an observer located $\Theta_{obs} = -35°$ below the rotor plane at a radial distance of $y = 11.94R$ away from the center of the rotor.

The APTH calculated using ACAPT from the ten revolutions of sampled data was then separated into ten equally sized blocks correspondent to each revolution of rotor data. These ten revolutions of data were averaged together to obtain a mean revolution of APTH, which is the periodic (i.e., tonal) noise signal. This tonal noise signal was then subtracted from the raw, aperiodic APTH from the ten revolutions of data and the resultant residual APTH served as the stochastic (i.e., broadband) noise signal.

The mean rotor revolution of predicted data was repeated enough times to attain a Δf = 20 Hz frequency resolution, which was then processed by treating the repeated rotor revolution data as an aperiodic signal, computing the fast Fourier transform (FFT) of the data, then using Eq. (1) to produce a narrowband spectrum of the predicted tonal noise sound pressure level (SPL);

$$\text{SPL} = 10\log_{10}\left(\frac{G_{xx} * \Delta\text{f}}{p_{ref}^2}\right), \tag{1}$$

where G_{xx} is the resultant power spectral density from the FFT calculation and $p_{ref} = 20\ \mu$Pa.

The extracted broadband noise signals from the computations were treated as aperiodic signals over which an FFT was also calculated using ten blocks, or one block per revolution of residual APTH data, with a spectral resolution of Δf = 91.68 Hz. Equation (1) was used to produce narrowband broadband noise SPL values, which were then used to generate one-third octave band ($\text{SPL}_{1/3}$) representations. A logarithmic representation of the resultant computational broadband G_{xx} values from the FFT calculation was also generated using the following:

$$\text{PSD} = 10\log_{10}\left(\frac{G_{xx}}{p_{ref}^2}\right). \tag{2}$$

Similar acoustic processing techniques were used for the experimental data measured in the SHAC facility at the NASA Langley Research Center.

ANOPP2 was also used to generate on-surface metadata, or the acoustic contribution of each F1A integrand evaluated over each surface element. Since no quadrupole terms are used by the impermeable F1A calculation, the broadband noise contribution to the APTH data is primarily contained in the unsteady loading term of F1A:

$$p'_{UL}(t_{obs}) = \frac{1}{4\pi}\int_{f=0}\left[\frac{\dot{p}cos\theta}{c_\infty r_d(1-M_r)^2}\right]_{ret} dS, \tag{3}$$

where the integral is evaluated over the surface, $f = 0$, in retarded, or emission, time, τ, denoted by the subscript, ret. In Eq. (3), $M_r = M \cdot \hat{\mathbf{r}}_d$ is the local Mach number in the direction of the observer located at $\mathbf{x}_{obs}$, $r_d = |\mathbf{x}_{obs} - \mathbf{y}_{src}|$ is the radiation distance between the observer and the acoustic source located at $\mathbf{y}_{src}$, and θ is the local angle between the surface normal vector, $\hat{\mathbf{n}}$, and the radiation direction, $\hat{\mathbf{r}}_d$.

For rotating systems, the tonal noise contribution inherently present in Eq. (3) due to Doppler effects may be excluded by selecting an acoustic observer collocated with the axis of rotation (i.e., constant r_d for each surface element).

In this fashion, Eq. (3) may be used to visualize broadband noise sources on a rotating surface in the time domain. The last post-processing technique used in this work leveraged Eq.(3) with an observer located directly above the center of the rotor at a radial distance of $y = 11.94R$ to produce temporal broadband noise source visualizations. The F1A calculation involves interpolating Eq. 3 from τ to observer time, t_{obs}, and it should be noted that the broadband noise source visualizations in Section III.C were evaluated in t_{obs}. This method for evaluating the on-surface acoustic contributions in observer time was introduced by Zawodny and Boyd [29], where the on-surface acoustic visualizations were denoted as Σ-surfaces.

III. Results

A. Aerodynamic Results

The computed thrust and torque values for all four cases simulated using OVERFLOW2 are compared against experimental measurements and PowerFLOW simulations from Ref. [8] in Table 2. It can be seen in the table that both

Table 2 Aerodynamic performance comparison at the design operating condition.

Case	Experiment	PowerFLOW	OVERFLOW2			
			Case 1	Case 2	Case 3	Case 4
Thrust	10.1 N	9.16 N	9.30 N	9.25 N	9.34 N	9.39 N
Relative Difference		9.31%	7.92%	8.42%	7.52%	7.03%
Torque	-0.210 N-m	-0.187 N-m	-0.209 N-m	-0.210 N-m	-0.209 N-m	-0.210 N-m
Relative Difference		10.95%	0.476%	0%	0.476%	0%

OVERFLOW2 and PowerFLOW predicted comparable thrust values with the experiment. The torque values predicted by OVERFLOW2 agreed much better with the experiment (< 0.5%) when compared to the PowerFLOW prediction (11%). This discrepancy in the predicted torque from PowerFLOW may be attributed to the code's use of algebraic wall-functions and isotropic grid cells in the boundary layer (i.e., $y^+ > 6$) [30], whereas OVERFLOW2 computes the boundary layer as fully turbulent using RANS-based turbulence models solved over stretched body-fitted grids with a first-cell spacing very near to the geometry (i.e., $y^+ = 0.3$). Comparing simulation cases, it can be seen that the torque predicted using SST-DDES in Case 2 compares better with the experiment than the baseline case; however, the thrust prediction is degraded. Out of the four simulation cases, the increased spatial resolution used in Case 4, produced the best thrust and torque predictions when compared to the experiment.

Since the focus of this work was on broadband BWI and BWBS noise, flow visualizations were produced using the baseline case to highlight the aerodynamic phenomena associated with broadband noise generation. Figure 5 shows isosurfaces of vorticity at two different values colored by pressure. As it can be seen in Fig. 5, there are no turbulent structures in the boundary layer implying that TBLTE and laminar boundary layer vortex shedding (LBLVS) noise cannot be predicted with the current methodology, which is a direct consequence of using RANS-based turbulence modeling. Figure 5 also shows three distinct regions thought to be associated with broadband noise generation. Region 1) shows the shedding of blade wake, where vortical structures aligned normal to the direction of cross-flow are apparent. Region 1) also shows that there is a pressure increase at the trailing edge associated with the shedding of blade wake. Region 2) shows the first perpendicular BVI, where Fig. 5a highlights the negligible vertical separation distance between the vortex core and the leading edge of the blade and Fig. 5b highlights the impingement of the blade wake entrained around the tip vortex on the blade leading edge. This blade wake impingement is associated with the broadband noise source, BWI noise. It can also be seen that there is a pressure increase in Region 2) associated with this blade wake impingement. Lastly, Region 3) shows that after leading edge impingement, the vortex-entrained blade wake convects along the blade, where it ultimately convects past the trailing edge of the blade and cause blade-wake back-scatter.

Figure 6 shows a detailed vorticity visualization of the blade wake shedding from Region 1) in Fig. 5 along a vertical slice aligned with the $r = 0.75R$ spanwise location. It should be noted that the $r = 0.75R$ spanwise location is inboard of the perpendicular BVI. The boundary layer is fully attached at this spanwise location and the shedding of blade wake from both the suction and pressure sides of the blade past the blunt trailing edge is seen to cause alternating vortex shedding (i.e., vortex street), which is associated with a Kelvin-Helmholtz instability. Four different time steps have been included in Fig. 6 to visualize this alternating vortex pattern which develops at the blade trailing edge in the near

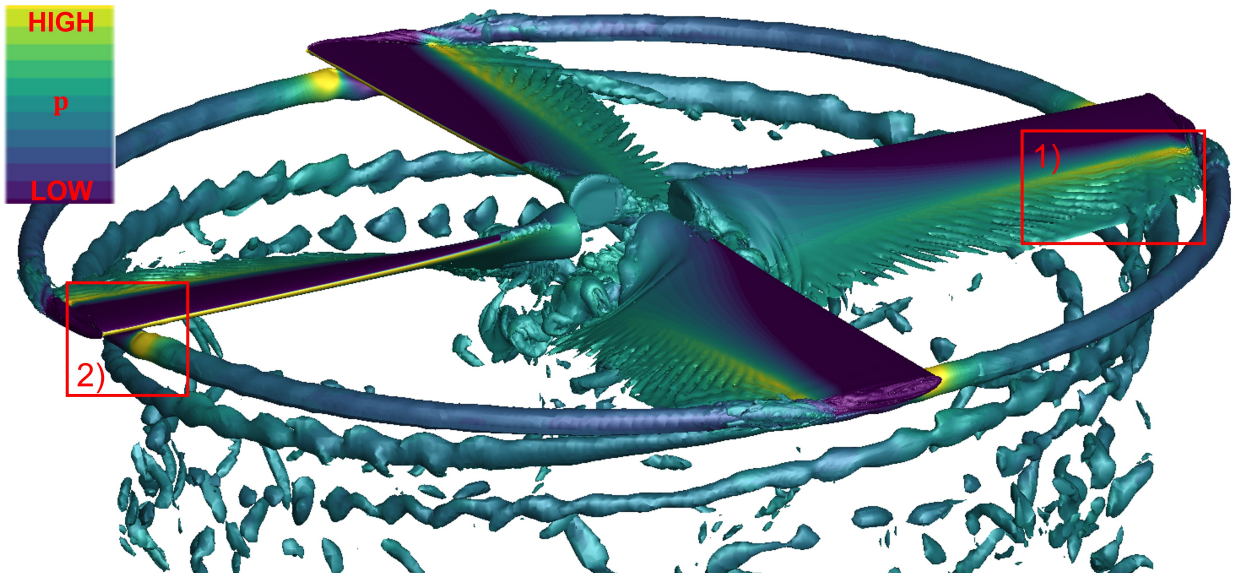

(a) $|\omega| = 5000/s$.

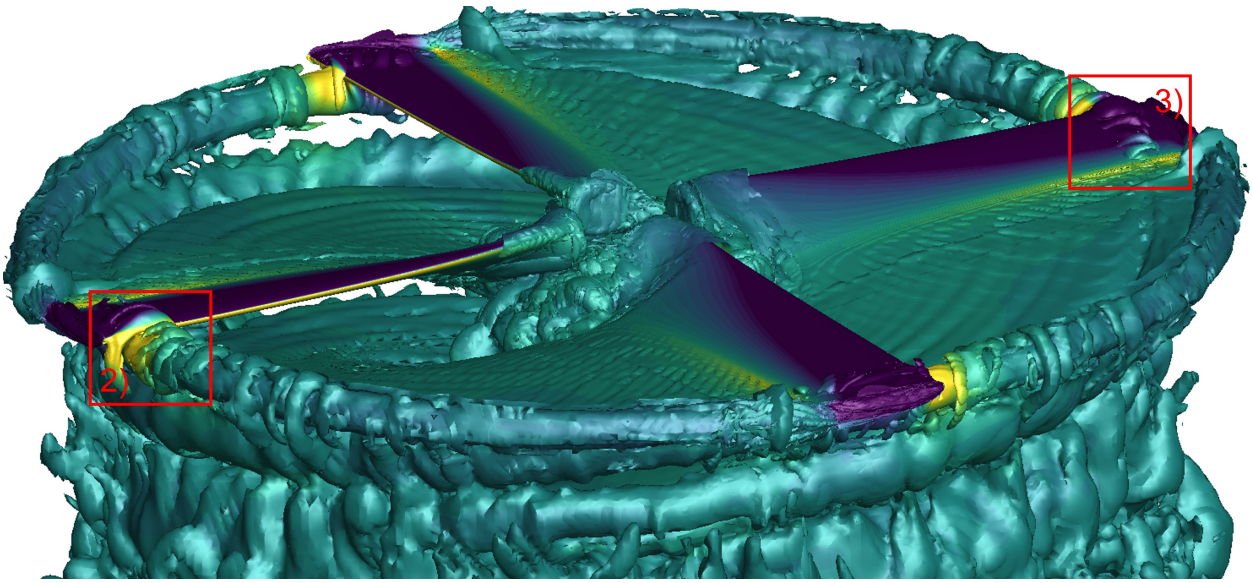

(b) $|\omega| = 1000/s$.

Fig. 5 Isosurfaces of vorticity magnitude colored by pressure where 1) shows the shedding of blade wake, 2) shows vortex impingement, and 3) shows blade wake convection along blade suction side.

wake. This alternating vortex shedding is known to be associated with the broadband self-noise source, bluntness vortex shedding (BVS) noise [4, 31, 32].

Figure. 7 shows vorticity visualizations at four different time steps on a vertical slice aligned with the trailing edge of a blade to illustrate the flow phenomena in Regions 2) and 3) from Fig. 5b more closely. These flow visualizations illustrate the tip vortex from a preceding blade after its impingement by a subsequent blade. As it can be seen, the vortex-entrained blade wake, or turbulent field, surrounding the vortex core has a swirl velocity associated with it and rotates about the core as it convects over the suction side of the blade. Momentum transfer between the first and second perpendicular BVIs can also be seen in Fig. 7, which is thought to be the vortex pairing or 'turbulent worms' first identified by Chaderjian [33, 34] and recently studied by Bodling [35].

Lastly, the temporal evolution of pressure waves associated with the flow phenomena in Regions 1), 2), and 3) of

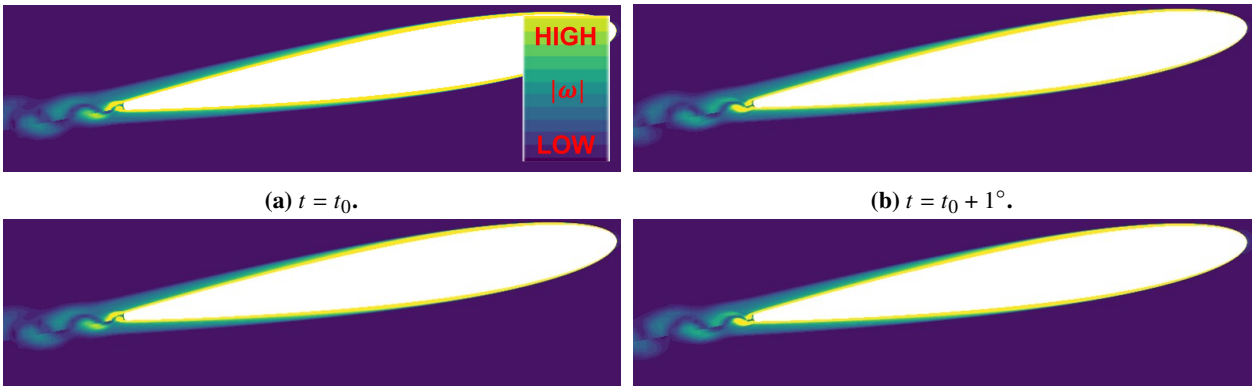

(a) $t = t_0$. **(b)** $t = t_0 + 1°$. **(c)** $t = t_0 + 2°$. **(d)** $t = t_0 + 3°$.

Fig. 6 Flow visualization of vorticity magnitude along spanwise slice at $r = 0.75R$ showing near-wake vortex shedding.

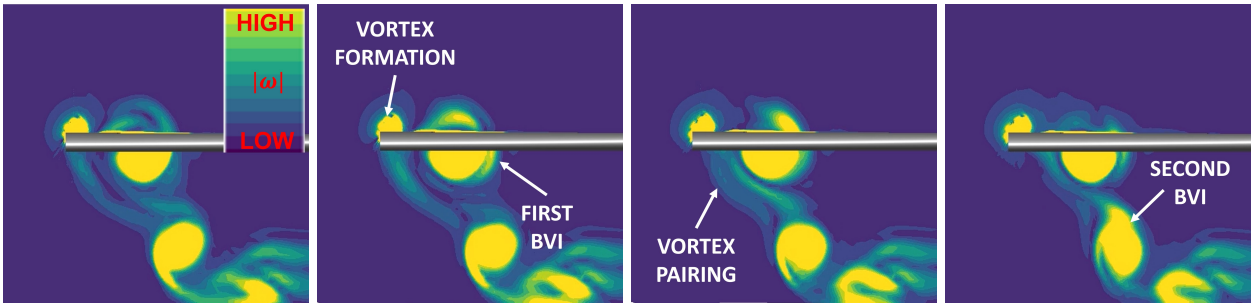

(a) $t = t_0$. **(b)** $t = t_0 + 1°$. **(c)** $t = t_0 + 2°$. **(d)** $t = t_0 + 3°$.

Fig. 7 Flow visualization of vorticity magnitude along trailing edge-aligned vertical slice showing impingement of vortex from previous blade.

Fig. 5 can be seen in Fig. 8 at four different time steps, where the blade suction and pressure sides are contoured by the time derivative of pressure. The time derivative of pressure is a good indication of acoustic emission since it is a key parameter in the unsteady loading noise term of F1A, or p'_{UL}, shown in Eq. (3). There are four things to note in Fig. 8, which have been labeled following the same convention used in Fig. 5. Region 1) shows the evanescent pressure back-scatter associated with the aforementioned near-wake vortex shedding phenomenon localized along the blade trailing edge. Region 2), at the leading edge of the blade, highlights the unsteady loading caused by the impingement of the turbulent field entrained by the tip vortex from a previous blade, which causes BWI noise. Region 3) shows two distinct pressure lobes along the outboard trailing edge, which are aligned with the locations of maximum upwash and downwash (i.e., leftmost and rightmost) of the blade wake entrained by the tip vortex. As this tip vortex-entrained blade wake convects past the trailing edge of the blade, significant blade-wake back-scatter is seen to occur on both the suction and pressure sides of the blade, where the pressure waves propagate in time from the trailing edge toward the leading edge along the chordwise direction. This phenomenon has not previously been identified and will hereby be denoted as blade-wake back-scatter, or BWBS. As it can be seen, this BWBS is the dominant flow feature in Fig. 8 and its broadband acoustic contribution will be investigated in Section III.C. Lastly, Region 4), which was not shown in Fig.5, shows the unsteady loading caused by tip vortex formation on the suction side of the blade near the tip region. The formation of tip vortices is known to cause a broadband self-noise source, tip vortex formation (TVF) noise [4].

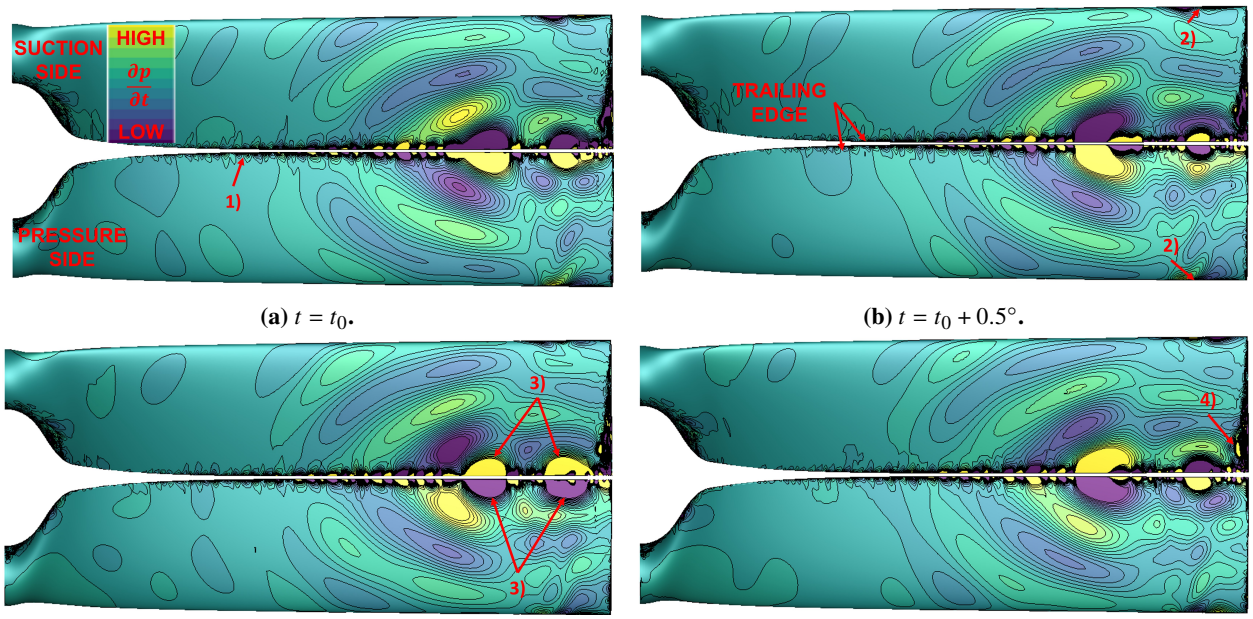

(a) $t = t_0$. **(b)** $t = t_0 + 0.5°$.

(c) $t = t_0 + 1°$. **(d)** $t = t_0 + 1.5°$.

Fig. 8 Time derivative of pressure on rotor blade surface.

B. Aeroacoustic Prediction Results

1. Case 1: Baseline

Tonal noise on an SPL basis and broadband noise, both on a PSD and $SPL_{1/3}$ basis, are shown in Fig. 9 for measured data as well as for results predicted with PowerFLOW and the baseline OVERFLOW2 case at the out-of-plane observer located $\Theta_{obs} = -35°$ below the rotor plane and $y = 11.94R$ away from the rotor. It can be seen in Fig. 9a that the

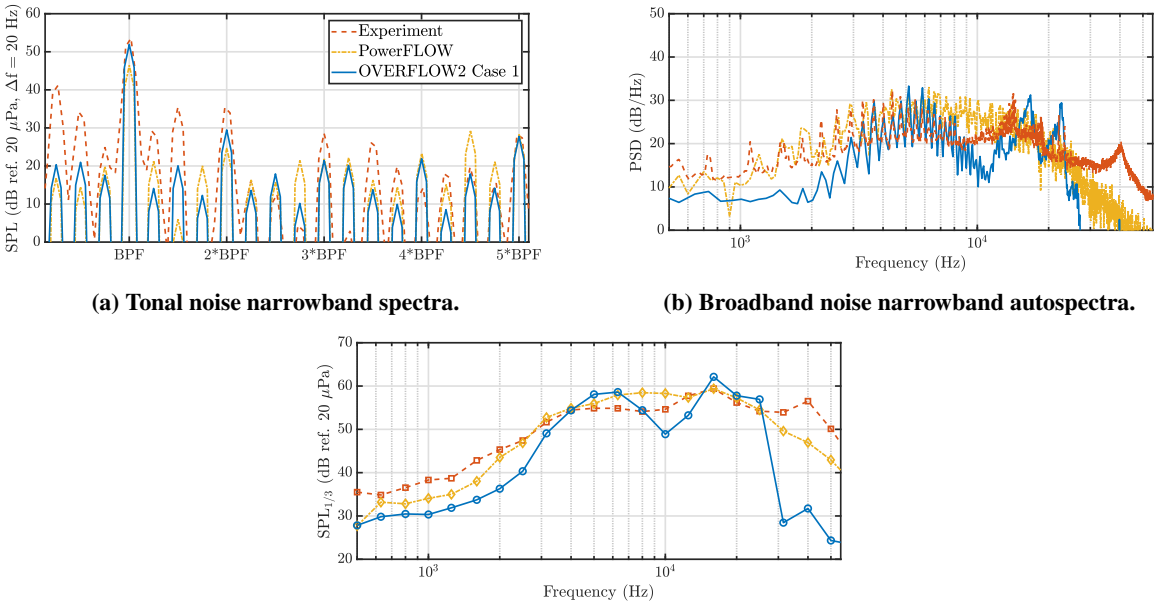

(a) Tonal noise narrowband spectra.

(b) Broadband noise narrowband autospectra.

(c) Broadband noise one-third octave spectra.

Fig. 9 Acoustic result comparison for Case 1 at the out-of-plane observer location ($\Theta_{obs} = -35°$, $y = 11.94R$).

baseline OVERFLOW2 tonal noise prediction agrees better than the PowerFLOW prediction at the fundamental and second harmonic of the BPF and that both predictions compare similarly to the measured data at the third through fifth harmonics of the BPF. It is also interesting to note the shaft harmonic excitation (i.e., 0.25*BPF, 0.5*BPF, 0.75*BPF, 1.25*BPF, etc.) predicted by both simulations. Typically, shaft harmonic excitation is indicative of blade-to-blade differences (e.g., mass imbalance, collective pitch variation); however, in a computational setting, these blade-to-blade differences don't exist. In the absence of blade-to-blade variation, the shaft harmonic excitation may be explained by aerodynamic loading differences between blades, shown in Figs. 4c and 4d.

As mentioned previously, the broadband self-noise sources, TBLTE and LBLVS, were not predicted by the hybrid RANS/LES approach used in this work or by PowerFLOW, which used wall-functions in the boundary layer. Even without the prediction of these noise sources, Fig. 9b shows good agreement between predicted and measured results, with better agreement between the PowerFLOW results and experiment. The baseline OVERFLOW2 case does predict the residual BPF tones between approximately 3 and 10 kHz apparent in the measured data; however, the amplitude of these residual tones is mispredicted, which is shown more clearly in Fig. 9c. Tones around 16 kHz and 21 kHz are also apparent in the OVERFLOW2 prediction, which roughly coincide with similar spectral behavior observed in the measured data. It should be noted that these residual tones are present in the 'tone-removed' APTH data and that the tonal thickness/loading noise components due to Doppler effects have been averaged out of the results shown in Fig. 9b. It was shown in Refs. [36] and [37] that these residual higher-harmonic BPF tones are typically associated with leading edge turbulence impingement and since the simulations were absent of atmospheric turbulence, the most likely cause of these residual tones is the leading edge interaction with blade wake entrained by the tip vortex from the preceding blade.

2. Case 2: Turbulence Model

Figure 10 compares the tonal and broadband noise between the measured data, Case 1, and Case 2, which uses the SST-DDES turbulence model. It can be seen in Fig. 10a that the different turbulence model used by Case 2 allows for slightly better tonal noise prediction at shaft harmonics and at the second and fourth BPF harmonics; however, the fundamental BPF prediction is identical between Cases 1 and 2. Case 2 also underpredicts the fifth BPF harmonic. The

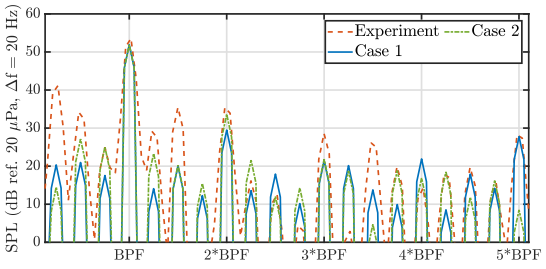

(a) Tonal noise narrowband spectra.

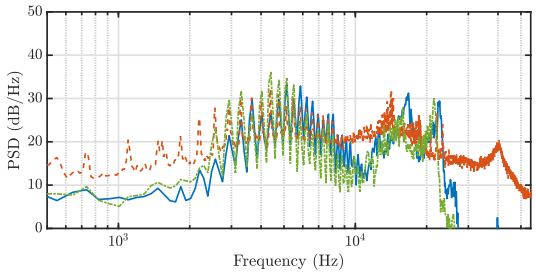

(b) Broadband noise narrowband autospectra.

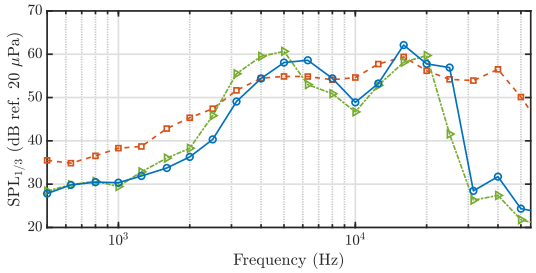

(c) Broadband noise one-third octave spectra.

Fig. 10 Acoustic result comparison for Case 2 at the out-of-plane observer location ($\Theta_{obs} = -35°$, $y = 11.94R$).

broadband noise prediction shown in Fig. 10b shows that Case 2 overpredicts the residual tones between 3 kHz and 5 kHz, whereas Case 1 overpredicts these residual tones between 5 kHz and 8 kHz, which can be seen more clearly in Fig. 10c. There are minor differences in the empirical RANS-to-LES blending function between SA-DDES and SST-DDES; however, once this RANS-to-LES switch occurs, the LES path between both Cases 1 and 2 is identical. The

improved tonal noise predictions from Case 2 may be due to a better boundary layer prediction by SST when compared with SA, which can be ascertained from the better torque prediction by Case 2 shown in Table 2.

3. Case 3: Temporal Resolution

Tonal and broadband noise predictions using an increased AMR and sampling resolution (Case 3) are compared with measurements and the baseline OVERFLOW2 case in Fig. 11. It can be seen in Fig. 11a that the fundamental and most BPF harmonics are predicted similarly between both Case 1 and 3; however, small differences between the two cases can be seen at the shaft harmonics. Figures 11b and 11c show very similar broadband noise predictions between the two

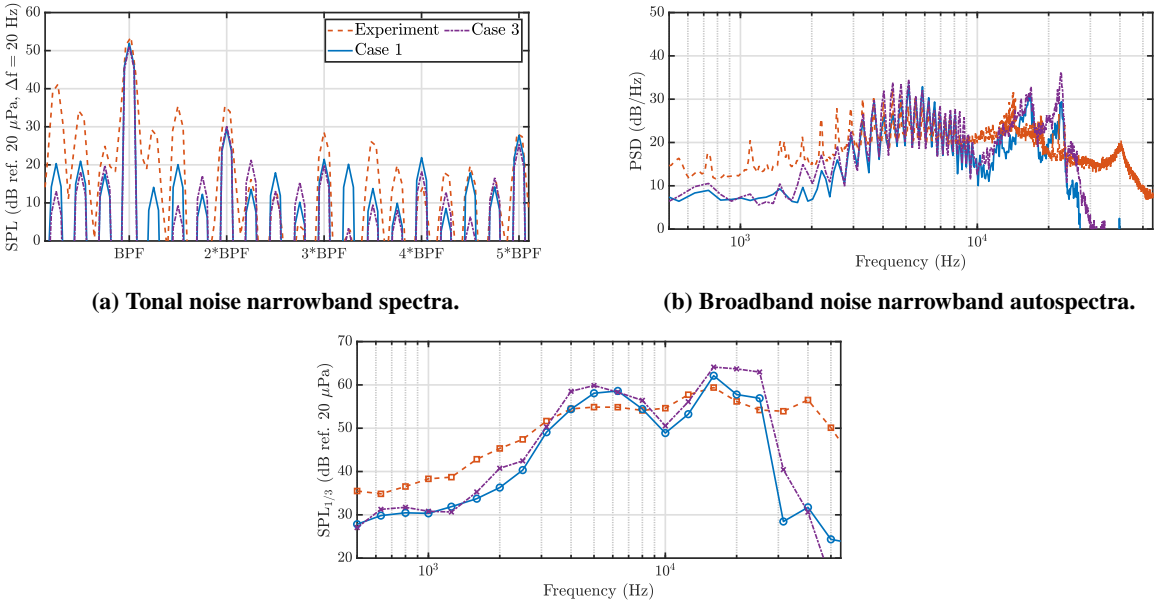

(a) Tonal noise narrowband spectra.

(b) Broadband noise narrowband autospectra.

(c) Broadband noise one-third octave spectra.

Fig. 11 Acoustic result comparison for Case 3 at the out-of-plane observer location ($\Theta_{obs} = -35°$, $y = 11.94R$).

cases, with the amplitudes of the two residual tones above 10 kHz being a bit higher for Case 3 than for Case 1. Since the CFD temporal resolution is identical between Cases 1 and 3, no additional flow physics are attained by increasing the sampling resolution. One may expect a better representation of the resolved flow features with the increased sample rate, which is clearly not the case. A better approach may have been to also increase the CFD temporal resolution, while retaining AMR and surface pressure sampling at every two time steps (i.e., $\Delta t = 0.125°$ and $\Delta t_s = 0.25°$). The results presented in this section indicate that the common practice of using AMR and sampling surface pressures every two time steps rather than every time step may be a better approach in terms of both computational efficiency and acoustic predictions.

4. Case 4: Spatial Resolution

Figure 12 compares the tonal and broadband noise predicted using increased spatial resolution against the baseline OVERFLOW2 case and measured data. It should be noted that the near-body blade grids are identical between Cases 1 and 4 and only the first off-body grid and AMR regions were spatially refined by Case 4. It can be seen in Fig. 12a that both computational cases predict the fundamental BPF almost identically; however, Case 4 underpredicts the second BPF harmonic overpredicts the fourth BPF harmonic. The third and fifth BPF harmonics also appears similar between both simulation cases, as well as most shaft harmonics. It can be seen in Fig. 12c that Case 4 produced the best broadband noise prediction out of the four cases in this work when compared to the measured data. Figure 12b shows that Case 4 accurately predicts the residual tone peaks below 6 kHz but overpredicts all troughs between the residual tones. Since grid refinement was only used in the off-body grids, the LES region of the computational domain is able to resolve smaller flow features, which would in turn increase the rate of turbulent diffusion. It is believed that the smaller-scale turbulent structures surrounding the tip vortex, coupled with a larger turbulent field due to the increased

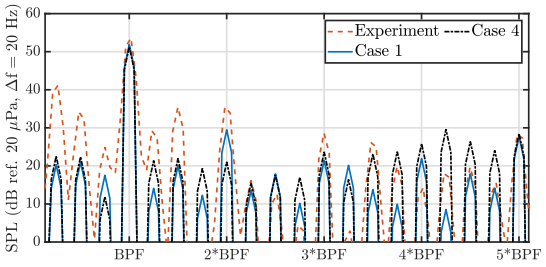

(a) Tonal noise narrowband spectra.

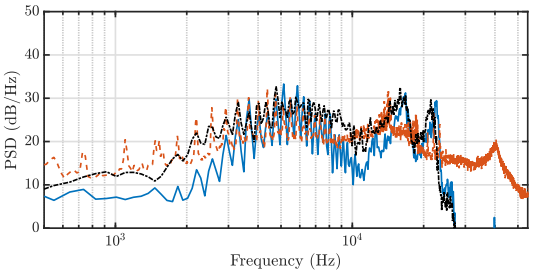

(b) Broadband noise narrowband autospectra.

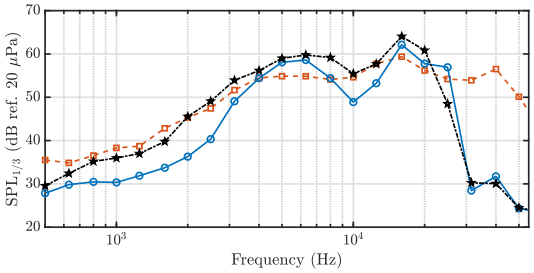

(c) Broadband noise narrowband autospectra.

Fig. 12 Acoustic result comparison for Case 4 at the out-of-plane observer location ($\Theta_{obs} = -35°$, $y = 11.94R$).

diffusion may explain the broadband noise spectral differences between Case 4 and Case 1 seen in Fig. 12b.

C. Broadband Noise Source Visualization

Figure 13 shows the temporal evolution of the unsteady loading term of Farassat's F1A, or p'_{UL} in Eq. (3), evaluated in observer time, t_{obs}. Though the flow visualizations in Section III.A provided a good indication of the aerodynamic phenomena associated with broadband noise generation, Fig. 13 provides a true acoustic source representation of the broadband noise on both the suction and pressure sides of the blade, as a microphone placed directly overhead of the rotor at $y = 11.94R$ would observe. Similar to the pressure time derivative visualization shown in Fig. 8, BWBS appears to be the dominant broadband noise source shown in Fig. 13. This noise source can be characterized by the two out-of-phase lobes of unsteady acoustic loading at the trailing edge of the blade, aligned with the locations of maximum upwash/downwash of the tip vortex-entrained blade wake as it convects along the blade. It should be noted that this tip vortex-entrained blade wake has no acoustic contribution during its convection along the blade. As this blade wake convects past the trailing edge of a blade, it causes significant back-scatter, which propagates in time from the trailing edge toward the leading edge of both the suction and pressure sides of the blade.

Inboard of this BWBS in Fig. 13, evanescent back-scatter caused by the near-wake vortex shedding, or BVS, can be observed on both sides of the blade. Both trailing edge broadband noise sources, BWBS and BVS, appear to be symmetric about the blade chord in Fig. 13, with very similar propagation patterns along the suction and pressure sides of the blade. Outboard of the BWBS, at the blade tip region of the blade suction side, TVF can be seen to occur. It is difficult to discern from Fig. 13 whether there is any leading edge broadband noise generation associated with BWI or if the unsteady loading seen at the leading edge is caused by the BWBS.

IV. Conclusions

This work investigated broadband noise prediction using a hybrid RANS/LES approach implemented in the structured Navier-Stokes solver, OVERFLOW2. The ideally twisted rotor geometry was simulated at its baseline hovering condition, rotating at $\Omega = 5500$ RPM. Results using turbulence models and spatiotemporal resolutions were compared against experimental measurements and previous simulation results obtained using the lattice-Boltzmann code, PowerFLOW. It was shown that increasing the spatial resolution in the first off-body grid and AMR region (Case 4) produced the best rotor performance predictions, which underpredicted the measured thrust by approximately

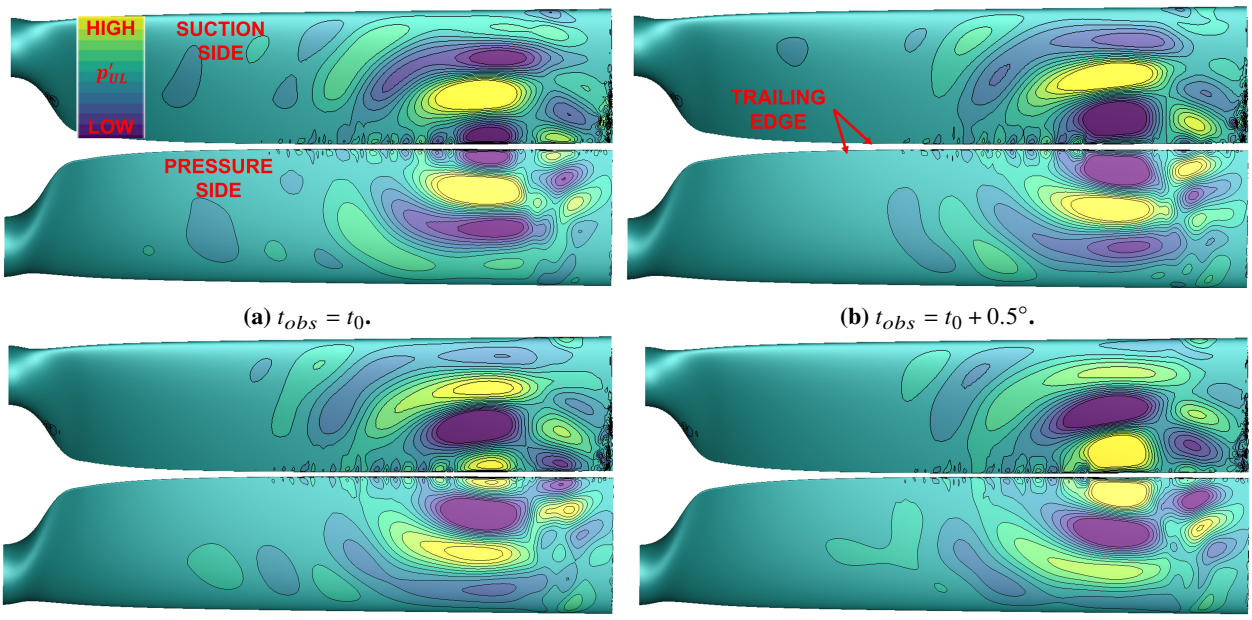

(a) $t_{obs} = t_0$. **(b)** $t_{obs} = t_0 + 0.5°$.

(c) $t_{obs} = t_0 + 1°$. **(d)** $t_{obs} = t_0 + 1.5°$.

Fig. 13 Unsteady loading term of Farassat's F1A equation in observer time, t_{obs}, calculated directly above the rotor ($\Theta_{obs} = 90°$, $y = 11.94R$).

7% with no relative difference between predicted and measured torque. It was also shown that this increased spatial resolution case produced the best broadband noise prediction when compared to the other three cases in this work; however, the second BPF harmonic was underpredicted and the fourth BPF harmonic was overpredicted when compared to the measured data. All simulation cases agreed favorably with the measured torque prediction when compared to the PowerFLOW results, which could be attributed to PowerFLOW's use of wall-functions and isotropic cells in the boundary layer. The SST-DDES simulation case (Case 2) predicted torque and tonal noise slightly better than the SA-DDES used by the baseline simulation case when compared to the measured data.

Flow visualizations of the baseline simulation case were used to identify flow features associated with broadband noise generation. The first of these identified flow features was vortex shedding caused by a Kelvin-Helmholtz instability from the mixing of suction and pressure side shear layers in the near-wake region of the blade, just aft of the blunt trailing edge. This form of near-wake vortex shedding is known to be associated with a type of broadband self-noise, bluntness vortex shedding. Another flow feature identified was leading edge impingement of the blade wake entrained by the tip vortex from a preceding blade, which causes broadband BWI noise. After leading edge impingement, this tip vortex-entrained blade wake convects along the blade until it traverses the trailing edge. Once this blade wake convects past the trailing edge, it causes significant back-scattering of pressure waves along both the suction and pressure sides of the blade, which is the dominant flow mechanism for the newly introduced broadband noise source, blade-wake back-scatter. Unsteady loading associated with the broadband self-noise source, tip vortex formation noise, was also shown.

Lastly, a method for broadband noise source visualization was used where the unsteady loading term of Farassat's F1A, calculated in observer time at an overhead location (i.e., no Doppler effects), was evaluated on the blade surface. This broadband noise source visualization largely confirmed the presence of blade-wake back-scatter as a dominant broadband noise source. This blade-wake back-scatter was characterized by two out-of-phase acoustic pressure lobes originating at the blade trailing edge and propagating toward the leading edge of both suction and pressure sides of the blade in a symmetric fashion. Inboard and outboard of this blade-wake back-scatter, bluntness vortex shedding noise and tip vortex formation noise were also identified, respectively.

V. Acknowledgments

The authors would like to thank Nikolas Zawodny and Nicole Pettingill from the Aeroacoustics Branch at the NASA Langley Research Center for their invaluable role in providing experimental measurements used for comparison in this work. This work was funded by the NASA Revolutionary Vertical Lift Technology (RVLT) project. Computational resources supporting this work were provided by the Midrange HPC K-Cluster at the NASA Langley Research Center.

References

[1] Zawodny, N. S., Boyd Jr., D. D., and Burley, C. L., "Acoustic Characterization and Prediction of Representative, Small-Scale Rotary-Wing Unmanned Aircraft System Components," *AHS International 72nd Annual Forum & Technology Display*, West Palm Beach, FL, May 2016.

[2] Thurman, C. S., Zawodny, N. S., and Baeder, J. D., "Computational Prediction of Broadband Noise from a Representative Small Unmanned Aerial System Rotor," *VFS International 76th Annual Forum & Technology Display*, Virtual, October 2020.

[3] Amiet, R., "Acoustic Radiation from an Airfoil in a Turbulent Stream," *Journal of Sound and Vibration*, Vol. 41, No. 4, 1975, pp. 407–420.

[4] Brooks, T. F., Pope, D. S., and Marcolini, M. A., "Airfoil Self-Noise and Prediction," NASA RP 1218, 1989.

[5] Li, S., and Lee, S., "UCD-QuietFly: A New Program to Predict Multi-Rotor eVTOL Broadband Noise," *2020 VFS Aeromechanics for Advanced Vertical Flight Technical Meeting*, San Jose, CA, January 2020.

[6] Burley, C. L., and Brooks, T. F., "Rotor Broadband Noise Prediction with Comparison to Model Data," *Journal of the American Helicopter Society*, Vol. 49, No. 1, 2004, pp. 28–42.

[7] Pettingill, N. A., and Zawodny, N. S., "Identification and Prediction of Broadband Noise for a Small Quadcopter," *VFS International 75th Annual Forum & Technology Display*, Philadelphia, PA, May 2019.

[8] Thurman, C. S., Zawodny, N. S., Pettingill, N. A., Lopes, L. V., and Baeder, J. D., "Physics-informed Broadband Noise Source Identification and Prediction of an Ideally Twisted Rotor," *AIAA SciTech 2021 Forum*, AIAA Paper 2021–1925, Virtual, January 2021.

[9] Pettingill, N. A., Zawodny, N. S., Thurman, C. S., and Lopes, L. V., "Acoustic and Performance Characteristics of an Ideally Twisted Rotor in Hover," *AIAA SciTech 2021 Forum*, AIAA Paper 2021–1928, Virtual, January 2021.

[10] Thurman, C. S., and Zawodny, N. S., "Aeroacoustic Characterization of Optimum Hovering Rotors using Artificial Neural Network," *VFS International 77th Annual Forum & Technology Display*, Virtual, May 2021.

[11] Fleming, J., Langford, M., Gold, J., Schwartz, K., Wisda, D., Alexander, N., and Whelchel, J., "Measured Acoustic Characteristics of Low Tip Speed eVTOL Rotors in Hover," *VFS International 78th Annual Forum & Technology Display, Fort Worth, TX*, May 2022.

[12] Ffowcs Williams, J. E., and Hawkings, D. L., "Sound Generation by Turbulence and Surfaces in Arbitrary Motion," *Philosophical Transactions of the Royal Society of London. Series A, Mathematical and Physical Sciences*, Vol. 264, No. 1151, 1969, pp. 321–342.

[13] Thurman, C. S., Zawodny, N. S., and Pettingill, N. A., "The Effect of Boundary Layer Character on Stochastic Rotor Blade Vortex Shedding Noise," *VFS International 78th Annual Forum & Technology Display*, Fort Worth, TX, May 2022.

[14] Thurman, C. S., "Computational Study of Boundary Layer Effects on Stochastic Rotor Blade Vortex Shedding Noise," *Aerospace Science and Technology*, Vol. 131A, No. 107983, 2022.

[15] Casalino, D., Romani, G., Zhang, R., and Chen, H., "Lattice-Boltzmann Calculations of Rotor Aeroacoustics in Transitional Boundary Layer Regime," *Aerospace Science and Technology*, Vol. 130, No. 107953, 2022.

[16] Chan, W. M., Gomez, R. J., Rogers, S. E., and Buning, P. G., "Best Practices in Overset Grid Generation," *32nd AIAA Fluid Dynamics Conference and Exhibit*, AIAA Paper 2002–3191, St. Louis, MO, June 2002.

[17] Buning, P. G., and Pulliam, T. H., "Cartesian Off-Body Grid Adaption for Viscous Time-Accurate Flow Simulation," *20th AIAA Computational Fluid Dynamics Conference*, AIAA Paper 2011–3693, Honolulu, HI, June 2011.

[18] Benek, J. A., Buning, P. G., and Steger, J. L., "A 3-D CHIMERA Grid Embedding Technique," *7th Computational Physics Conference*, AIAA Paper 85–1523, Cincinnati, OH, July 1985.

[19] Nichols, R. H., Tramel, R. W., and Buning, P. G., "Solver and Turbulence Model Upgrades to OVERFLOW 2 for Unsteady and High-Speed Applications," *24th Applied Aerodynamics Conference*, AIAA Paper 2006–2824, San Francisco, CA, June 2006.

[20] Chaderjian, N. M., "Quantitative Approach for the Accurate CFD Simulaton of Hover in Turbulent Flow," *Journal of the American Helicopter Society*, Vol. 68, No. 4, 2023, pp. 42009–42028.

[21] Tramel, R. W., Nichols, R. H., and Buning, P. G., "Addition of Improved Shock-Capturing Schemes to OVERFLOW 2.1," *19th AIAA Computational Fluid Dynamics Conference*, AIAA Paper 2009–3988, San Antonio, TX, June 2009.

[22] Derlaga, J. M., Jackson, C. W., and Buning, P. G., "Recent Progress in OVERFLOW Convergence Improvements," *AIAA SciTech 2020 Forum*, AIAA Paper 2020–1045, Orlando, FL, January 2020.

[23] Spalart, P. R., Deck, S., Shur, M. L., Squires, K. D., Strelets, M. K., and Travin, A., "A New Version of Detached-eddy Simulation, Resistant to Ambiguous Grid Densities," *Theoretical and Computational Fluid Dynamics*, Vol. 20, 2006, pp. 181–195.

[24] Gritskevich, M. S., Garbaruk, A. V., Schütze, J., and Menter, F. R., "Development of DDES and IDDES Formulations for the $k-\omega$ Shear Stress Transport Model," *Flow, Turbulence, and Combustion*, Vol. 88, 2012, pp. 431–449.

[25] Lopes, L., and Burley, C., "ANOPP2 User's Manual: Version 1.2," NASA TM 2016-219342, 2016.

[26] Farassat, F., and Succi, G. P., "The Prediction of Helicopter Discrete Frequency Noise," *Vertica*, Vol. 7, No. 4, 1983, pp. 309–320.

[27] Brentner, K., and Farassat, F., "Modeling Aerodynamically Generated Sound of Helicopter Rotors," *Progress in Aerospace Sciences*, Vol. 39, No. 2–3, 2003, pp. 83–120.

[28] Lopes, L., "ANOPP2's Farassat Formulations Internal Functional Modules (AFFIFMs) Reference Manual," NASA TM 2021-0021111, 2021.

[29] Zawodny, N. S., and Boyd, D. D., "Investigation of Rotor–Airframe Interaction Noise Associated with Small-Scale Rotary-Wing Unmanned Aircraft Systems," *Journal of the American Helicopter Society*, Vol. 65, No. 1, 2020, pp. 1–17.

[30] Brehm, C., Browne, O., and Ashton, N., "Towards a Viscous Wall Model for Immersed Boundary Methods," *2018 AIAA Aerospace Sciences Meeting*, AIAA Paper 2018–1560, Kissimmee, FL, January 2018.

[31] Brooks, T. F., and Hodgson, T. H., "Trailing Edge Noise Prediction from Measured Surface Pressures," *Journal of Sound and Vibration*, Vol. 78, No. 1, 1981, pp. 69–117.

[32] Tam, C. K. W., and Ju, H., "Aerofoil Tones at Moderate Reynolds Number," *Journal of Fluid Mechanics*, Vol. 690, 2012, pp. 536–570.

[33] Chaderjian, N. M., and Buning, P. G., "High Resolution Navier-Stokes Sumulation of Rotor Wakes," *AHS International 67th Annual Forum & Technology Display*, Virginia Beach, VA, May 2011.

[34] Chaderjian, N. M., "Advances in Rotor Performance and Turbulent Wake Simulations using DES and Adaptive Mesh Refinement," *Seventh International Conference on Computational Fluid Dynamics*, Kamuela, HI, July 2012.

[35] Bodling, A., Schwarz, C., Wolf, C. C., and Gardner, A. D., "Numerical and Experimental Assessment of Parameters Influencing the Development of Secondary Vortex Structures in Rotor Wakes," *VFS International 79th Annual Forum & Technology Display*, West Palm Beach, FL, May 2023.

[36] Amiet, R. K., "Noise Produced by Turbulent Flow into a Propeller or Helicopter Rotor," *AIAA Journal*, Vol. 15, No. 3, 1977, pp. 307–308.

[37] Paterson, R. W., and Amiet, R. K., "Noise of a Model Helicopter Rotor Due to Ingestion of Turbulence," NASA CR 3213, 1979.